

# THE CONNECTION BETWEEN THE CIRCUMGALACTIC MEDIUM AND THE INTERSTELLAR MEDIUM OF GALAXIES: RESULTS FROM THE COS-GASS SURVEY

SANCHAYEETA BORTHAKUR

Department of Physics & Astronomy, Johns Hopkins University, Baltimore, MD, 21218, USA and The Astronomy Department, University of California, Berkeley, CA USA

TIMOTHY HECKMAN

Department of Physics & Astronomy, Johns Hopkins University, Baltimore, MD, 21218, USA

JASON TURLINSON, RONGMON BORDOLOI, CHRISTOPHER THOM  
Space Telescope Science Institute, Baltimore, MD 21218, USA

BARBARA CATINELLA

Centre for Astrophysics & Supercomputing, Swinburne University of Technology, Hawthorn, VIC 3122, Australia

DAVID SCHIMINOVICH

Department of Astronomy, Columbia University, New York, NY 10027, USA

ROMEEL DAVÉ

University of the Western Cape, Bellville, Cape Town 7535,  
South Africa, South African Astronomical Observatories, Observatory, Cape Town 7925,  
South Africa, African Institute for Mathematical Sciences, Muizenberg, Cape Town 7945, South Africa

GUINEVERE KAUFFMANN

Max-Planck Institut für Astrophysik, D-85741 Garching, Germany

SEAN M. MORAN

Harvard-Smithsonian Center for Astrophysics, 60 Garden Street, Cambridge, MA 02138

AMELIE SAINTONGE

Department of Physics and Astronomy, University College London, Gower Place, London WC1E 6BT, UK

*Accepted for publication in ApJ*

## ABSTRACT

We present a study exploring the nature and properties of the Circum-Galactic Medium (CGM) and its connection to the atomic gas content in the interstellar medium (ISM) of galaxies as traced by the HI 21 cm line. Our sample includes 45 low- $z$  (0.026-0.049) galaxies from the GALEX Arecibo SDSS Survey. Their CGM was probed via absorption in the spectra of background Quasi-Stellar Objects at impact parameters of 63 to 231 kpc. The spectra were obtained with the Cosmic Origins Spectrograph aboard the Hubble Space Telescope. We detected neutral hydrogen ( $\text{Ly}\alpha$  absorption-lines) in the CGM of 92% of the galaxies. We find the radial profile of the CGM as traced by the  $\text{Ly}\alpha$  equivalent width can be fit as an exponential with a scale length of roughly the virial radius of the dark matter halo. We found no correlation between the orientation of sightline relative to the galaxy major axis and the  $\text{Ly}\alpha$  equivalent width. The velocity spread of the circumgalactic gas is consistent with that seen in the atomic gas in the interstellar medium. We find a strong correlation (99.8% confidence) between the gas fraction ( $M(\text{HI})/M_\star$ ) and the impact-parameter-corrected  $\text{Ly}\alpha$  equivalent width. This is stronger than the analogous correlation between corrected  $\text{Ly}\alpha$  equivalent width and  $\text{SFR}/M_\star$  (97.5% confidence). These results imply a physical connection between the H I disk and the CGM, which is on scales an order-of-magnitude larger. This is consistent with the picture in which the H I disk is nourished by accretion of gas from the CGM.

*Subject headings:* galaxies: halos — galaxies: ISM — quasars: absorption lines

## 1. INTRODUCTION

In the standard paradigm, galaxies grow primarily through the accretion of gas that flows from the Inter-Galactic Medium (IGM). Much of this accreted gas is ultimately turned into new stars. In turn, the massive stars

release matter and energy that can affect not only the galaxy itself, but also the IGM. These flows in and out of galaxies pass through the Circum-Galactic Medium (CGM), a region extending out from the galaxy itself to roughly the virial radius of the surrounding dark matter halo. The CGM also represents a significant reservoir of baryons (Werk et al. 2014; Stocke et al. 2013a). Thus, understanding the properties of the CGM is critical to understanding how galaxies and the IGM co-evolve.

The low densities in the CGM imply that it is very difficult to study in emission. Our ability to study the CGM in the present-day universe has been dramatically improved with the installation of the Cosmic Origins Spectrograph (COS) on the Hubble Space Telescope (HST). This has enabled us to use the rich suite of absorption-lines due to resonance transitions of many important atoms and ions that are present in the vacuum ultraviolet. Indeed, over the last few years, studies such as the COS-Halos, COS-Dwarfs, and others (Tumlinson et al. 2011a; Tripp et al. 2011; Prochaska et al. 2011; Borthakur et al. 2013; Tumlinson et al. 2013; Stocke et al. 2013a; Werk et al. 2014; Bordoloi et al. 2014; Liang & Chen 2014; Johnson et al. 2015) have established the connection between the CGM and many of the key properties of galaxies such as star-formation rate (SFR), stellar mass, color etc.

However, so far we have yet to explore the connection between the interstellar medium (ISM) and the CGM. This is important because in the simplest picture we would expect that incoming gas from the CGM would be largely ionized (e.g. Werk et al. 2014) and upon accretion would then have to pass through an HI phase and then a molecular phase before being converted into stars. Thus, the first step in assessing the role of accretion from the CGM in the evolution of galaxies would be to look at the relationship between the properties of the CGM and of the atomic gas in the galaxy disk.

Of particular interest in this context is a better understanding of the processes that produce a clear bimodality between the population of lower mass galaxies undergoing significant star-formation and higher mass quiescent galaxies. First discovered at low-redshift (e.g. Kauffmann et al. 2003; Blanton et al. 2003; Baldry et al. 2004), this split into a blue star-forming main sequence and a red and dead population is now known to be in place out to redshifts of two and beyond (e.g. Elbaz et al. 2011; Whitaker et al. 2013). The galaxy bimodality suggests that galaxies undergo fundamental changes (through accretion and merging) in their gas content and their ability to form new stars after either the galaxy itself or its dark matter halo exceeds a critical mass limit (e.g. Lilly et al. 2013). This quenching of star formation may be related to a change in the nature of the CGM, from a pathway for rapid ( $v_{in} \sim v_{vir}$ ) accretion of relatively cold gas ( $T \ll T_{virial}$ ) to slow and inefficient accretion of hot gas ( $T \sim T_{virial}$ ) mediated by radiative cooling (e.g. Kereš et al. 2005, 2009; Dekel et al. 2009).

To help probe the processes responsible for the drastic drop in star formation in massive galaxies and the implied change in the cold gas supply, we have undertaken the GALEX Arecibo SDSS Survey (GASS; Catinella et al. 2010). The GASS project combines 21 cm H I spectroscopic data obtained with the Arecibo

telescope, optical images and spectroscopy from the Sloan Digital Sky Survey (SDSS), and ultraviolet(UV) imaging with the Galaxy Evolution Explorer (GALEX) to measure the atomic gas and stellar content (star formation rate and history), gas phase metallicity, stellar morphology, and disk rotation speeds of about one thousand galaxies over the stellar mass range from  $M_* \sim 10^{10.0-11.5} M_\odot$  (roughly centered on the transition mass between star-forming and quiescent populations). We have also obtained molecular gas data from IRAM (COLD GASS; Saintonge et al. 2011) and long-slit optical spectroscopy (Moran et al. 2012) for a portion of the GASS sample.

Our sample of galaxies in this paper was drawn from the GASS parent sample. This sample enables us to probe the connection between the ISM and CGM in  $L_*$  galaxies in a statistically significant manner for the first time. In addition, our sample is also complementary to the COS-Halos sample as both the samples probe galaxies of similar stellar masses. While COS-Halos probed the inner CGM, our sample extends the CGM coverage out to the virial radii. Detailed descriptions of our sample selection criteria, the COS observations, and data reduction are presented in Section 2. The results are presented in Section 3. Finally, we summarize our findings and discuss their implications in Section 4. The cosmological parameters used in this study are  $H_0 = 70 \text{ km s}^{-1} \text{ Mpc}^{-1}$ ,  $\Omega_m = 0.3$ , and  $\Omega_\Lambda = 0.7$ .

## 2. OBSERVATIONS

### 2.1. Sample: COS-GASS

Our sample of galaxies was derived from the GASS Survey. We have observed all the Quasi Stellar Object (QSO) that probe GASS galaxies within a projected separation from the galaxy (impact parameter) of  $\leq 250 \text{ kpc}$ . The limiting flux of the background QSO was selected to be GALEX Far-UV AB magnitude,  $FUV_{mag} \leq 19.0$ . This yielded an observed sample of 47 QSO/galaxy pairs. The observations of two of those sightlines were found to be unsuitable for this analysis. The first is a Broad Absorption-Line (BAL) QSO in which it is difficult to perform robust measurements of the absorption features associated with the target galaxy. The second sightline yields a damped Ly $\alpha$  system which subsequent observations show not to be directly associated with the primary GASS target. We will discuss this unique system in Borthakur et al. (in preparation). Hence for the remainder of the paper we concentrate on our final COS-GASS sample of 45 QSO sightlines probing the CGM of low- $z$  galaxies.

Figure 1 presents the distribution of our QSO sightlines as a function of impact parameter and orientation with respect to the target galaxy. The sightlines are marked with filled green circles. Those probing face-on galaxies being marked in lighter green. The average optical and H I disk sizes of the galaxies are shown blue and red respectively. The optical sizes for the galaxies were estimated from the SDSS photometric parameter,  $R_{90}$ . The physical size of the Arecibo beam (full width at half maximum, FWHM, of  $3.3'$ ) at the average redshift of 0.037 for our sample is shown as the yellow circle. The Arecibo beam covers the optical extent of every galaxy, but does not extend to the virial radius.

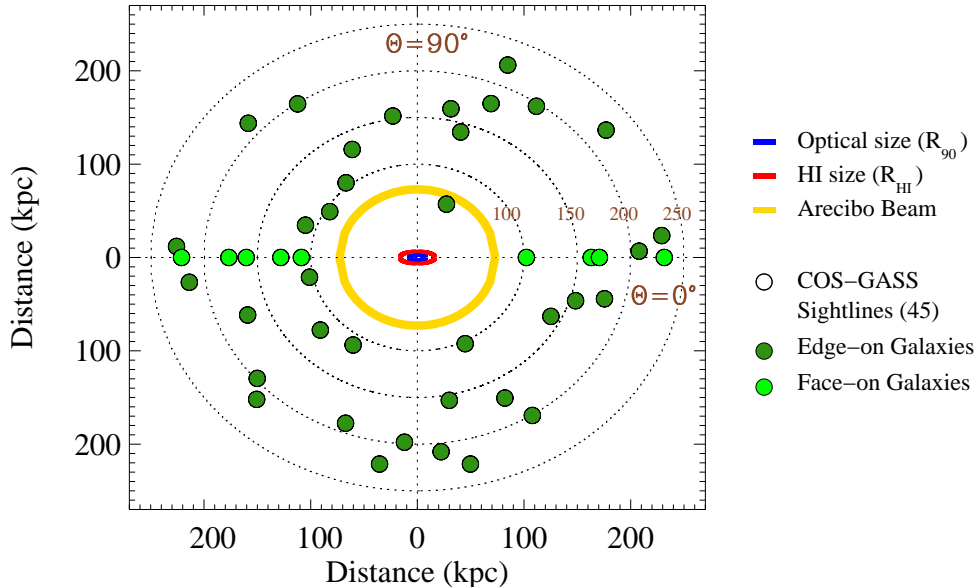


FIG. 1.— Overview of the COS-GASS sample. The figure shows a representative galaxy from the COS-GASS sample at the center of the plot and QSO sightlines shown as filled circles. The sample consists of 45 QSO-galaxy pairs probing the CGM in galaxies from the GASS project. The stellar masses of the sample galaxies range between  $10^{10.1-11.1} M_{\odot}$ . The median optical ( $R_{90}$ ) and HI radii ( $R_{\text{HI}}$ ) of the galaxies in the sample are shown as blue and red ellipses respectively at the center of the plot. The physical size corresponding to the FWHM of the Arecibo beam at 21 cm at the average redshift for our sample ( $\bar{z} = 0.037$ ) is shown in yellow. The QSO sightlines cover a range of impact parameters from 63-231 kpc. The position of the QSO sightlines with respect to the foreground galaxy are shown as filled green circles. The orientations of sightlines with respect to the disks are estimated using position angle of the galaxy major axis from SDSS photometry. We consider galaxies with de Vaucouleurs a/b parameter greater than 0.7 as having a face-on orientation. These galaxies were assigned an orientation parameter of zero degrees and are identified in this figure with a lighter shade of green.

The principal properties of the galaxies are summarized in Table 1. Except where noted below, these parameters are taken from the GASS project (see Catinella et al. 2010, 2012, 2013, for details). GASS also incorporates data products from the SDSS (Eisenstein et al. 2011). For example, position and redshift information are based on SDSS photometry and spectroscopic measurements respectively. The errors in the redshift measurements are of the order of  $10^{-4}$ , which corresponds to  $\sim 30 \text{ km s}^{-1}$ . The values are presented in Table 1 and have been rounded off to the fourth decimal place. The stellar masses of the galaxies in our sample range from  $10^{10.1-11.1} M_{\odot}$ . We estimated dark matter halo masses using the stellar mass measurements from GASS and the methodology described in Behroozi et al. (2010) (see Eq. 21 and Table 2). The halo masses were estimated for  $z=0$  (see for a detailed discussion Shull 2014) and they range from 11.6-13.3  $M_{\odot}$ . Based on these halo masses we estimated the virial radii. Our virial radius estimates are within 0.1 dex of those based on the luminosity based prescription in Prochaska et al. (2011). We report the halo masses and their corresponding virial radii in Table 1. The SFR and by extension the specific SFR ( $\text{sSFR} = \text{SFR}/M_{\star}$ ) for the GASS sample were derived using a combination of GALEX *FUV* and *NUV* and SDSS *u, g, r, i, z* photometry and SDSS spectral-line indices. (see section 2.2 of Schiminovich et al. 2010). Any value for  $\text{sSFR} < 10^{-12} \text{ yr}^{-1}$  can be regarded as an upper limit. We quote an uncertainty of 0.2 dex in  $\text{sSFR}$  for the galaxies with  $\text{sSFR} > 10^{-12} \text{ yr}^{-1}$ . These are based on results shown and discussed in detail by

Schiminovich et al. (2010). By including UV fluxes (from GALEX) in addition to  $\text{H}\alpha$  (from SDSS), the derived star formation rates are sensitive to timescales of the order of  $10^8$  yrs or larger. These rates define the recent star formation activity that might have impacted the CGM. For example, star-formation driven outflows traveling at  $200 \text{ km s}^{-1}$  would reach our closest sightline at an impact parameter of 63 kpc in about  $3 \times 10^8$  yrs and sightlines at impact parameter of 200 kpc in  $10^9$  yrs.

Information on the QSO sightlines is presented in Table 2. The azimuthal orientations of the QSO sightlines with respect to target galaxies were calculated from the position angle of the optical major axis of the galaxy from SDSS r-band photometry. We consider galaxies with the de Vaucouleurs AB parameter greater than 0.7 to be face-on and assign an orientation parameter of  $0^{\circ}$  in the analysis presented in the remainder of the paper.

## 2.2. HI masses from single-dish measurements

Our 21 cm H I spectroscopic data were primarily derived from the GASS observations obtained with the single-dish Arecibo telescope. The GASS sample also included a few galaxies from the Arecibo Legacy Fast ALFA (ALFALFA) Survey (Haynes et al. 2011) and Cornell H I archive (CHA, Springob et al. 2005) that met the GASS sample selection criteria. GASS HI parameters were measured by smoothing the H I profiles followed by a baseline subtraction. The edges and peaks of the H I profiles were interactively identified. Further details on the analysis procedures were described by Springob et al. (2005) and Catinella, Haynes & Giovanelli 2007 (AJ 134, 334). The velocities at zero flux

were marked interactively as part of the width and flux measurement process, at or near the position where the fits to the edges of the profile cross the baseline. The velocity widths were corrected for cosmological redshift and instrumental broadening using procedure described in Catinella et al. (2010). These measurements did not include corrections for effects due to inclination or turbulent motion. The measurements of H I masses and widths from the GASS database are included in Table 1.

For five galaxies in our sample, Arecibo H I measurements were not available (although they were members of the GASS parent sample). For these we performed similar observations with the Robert C. Byrd Green Bank Telescope (GBT)<sup>1</sup>. The GBT data were obtained under program GBT-14A-377. We used the dual polarization L-band system with two intermediate frequency (IF) modes and nine-level sampling. The IFs were set to yield a channel width of 1.56 kHz (0.33 km s<sup>-1</sup>) using 8192 channels over a total bandwidth of 12.5 MHz. Observations were made in the standard position-switching ON-OFF scheme with 300 s at each of the positions. Data were recorded at 10 s intervals to minimize the effect of RFI. The OFF position was chosen +20' offset in Right Ascension from each of the sight lines. During each of the observing sessions, we used one of the three standard flux calibrators 3C 48 (16.5 Jy), 3C 147 (22.5 Jy), and 3C 286 (15.0 Jy) - for pointing and estimating antenna gain. Local pointing corrections (LPCs) were performed using the observing procedure AutoPeak and the corrections were then automatically applied to the data. This should result in a pointing accuracy of 3". It is worth noting that the pointing accuracy does not signify the positional accuracy of the source of the H I flux. The H I emitting region may be present anywhere within the beam. The flux calibrations were performed by applying antenna gain to data for each session separately. Our calibration error is expected to be no more than 10%. The data were analyzed using the NRAO software GBTIDL.

The GBT observational setup was very similar to that of the GASS program and the data products were measured at the same spectral resolution as the GASS sample. The H I masses, the velocity widths and the origin of the H I data are presented in Table 1. The widths represent the full velocity extent of the features i.e. the width of the 21 cm transition at zero flux. The line-widths were estimated visually and the uncertainties associated with these values are typically  $\sim 20$  km s<sup>-1</sup>. The H I 21 cm velocity ranges cover the systemic velocity of the galaxy in all cases. We define the systemic velocity as the optical velocity that traces the stars. The stars represent the bulk of the measurable baryons in our galaxies. By doing so, we also alleviate the problem of identifying the systemic velocity from H I 21 cm profiles that may be asymmetric.

### 2.3. Cosmic Origins Spectrograph Observations

We carried out ultraviolet spectroscopic observations of the background QSOs with the COS aboard the HST. The data were obtained with the grating G130M of COS, providing a resolution  $R = 20,000$  -

24,000 (FWHM  $\sim 14$  km s<sup>-1</sup>). The data covered observed-frame wavelength of 1140-1470 Å. This included transitions such as Ly $\alpha$  ( $\lambda 1215.670$  Å), C II ( $\lambda 1334$  Å), Si II ( $\lambda 1190, 1193, \& 1260$  Å), Si III ( $\lambda 1206$  Å), Si IV ( $\lambda \lambda 1393, 1402$  Å), and O I ( $\lambda 1302$  Å).

The data were reduced using the standard COS pipeline. All absorption features in the spectra were identified and were exhaustively matched to identify the species and transition. Absorption features associated with the Milky Way, the target galaxies, intervening systems, and the background QSOs were identified. We use a velocity window of  $\pm 600$  km s<sup>-1</sup> with respect to the systemic velocity (based on SDSS redshifts) to associate absorption features with our target galaxies. In other words, transitions detected within  $\pm 600$  km s<sup>-1</sup> of the systemic velocity of the galaxies are assumed to be associated with the target galaxies. The large velocity window allows us to look for kinematic signatures of possible inflowing or outflowing material. Furthermore, the velocity window is same as used in the other large CGM studies such as COS-Halos (Tumlinson et al. 2013) and COS-Dwarfs (Bordoloi et al. 2014), thus making our analysis consistent with existing CGM studies.

We do miss a few transitions associated with the target galaxies due to blending with other absorption features such as from the Milky Way or intervening absorbers between the QSO and us. In this paper we focus on the Ly $\alpha$  transition probing the hydrogen in the CGM. A paper describing the metal line properties for the galaxies is in preparation. The Ly $\alpha$  equivalent width measurements are provided in column 9 of Table 2. We fitted Voigt profiles to the Ly $\alpha$  absorption features to estimate the velocity centroid of each of the components contributing to the full profile. Most of the Ly $\alpha$  absorption features (25/36) could be described with a single component. There are 10/36 Ly $\alpha$  absorption profiles that required two components and one that required three. The velocity centroids of all the components (listed in order of the strength of the component) and the entire widths of the Ly $\alpha$  absorption profiles within the rest-frame of the galaxy are also provided in Table 2.

## 3. RESULTS

We detected Ly $\alpha$  absorption in the CGM of 36 out of 39 galaxies where measurements could be made. In the remaining 6 sightlines, the data were contaminated by Milky Way or other intervening absorption systems. For the three non-detections, we report a limiting equivalent width that corresponds to 3 times the noise in the spectra in the vicinity of the expected transition. Most of the Ly $\alpha$  features are saturated (zero residual intensity in the line core) with an equivalent width of more than 0.3 Å.

### 3.1. Tracing the Circumgalactic Medium

We begin by assessing the connection of the detected Ly $\alpha$  absorbers to the CGM. Are we seeing gas that is physically connected to the galaxy (a true CGM) or simply material in the inter-galactic medium located close to the galaxy in projection?

First, we can compare the distribution of the Ly $\alpha$  absorbers with respect to the virial radius ( $R_{\text{vir}}$ ) of the dark matter halo. Our sightlines probe gas at impact parameters comparable to the  $R_{\text{vir}}$  (so, we sample mostly the

<sup>1</sup> The National Radio Astronomy Observatory is a facility of the National Science Foundation operated under cooperative agreement by Associated Universities, Inc.

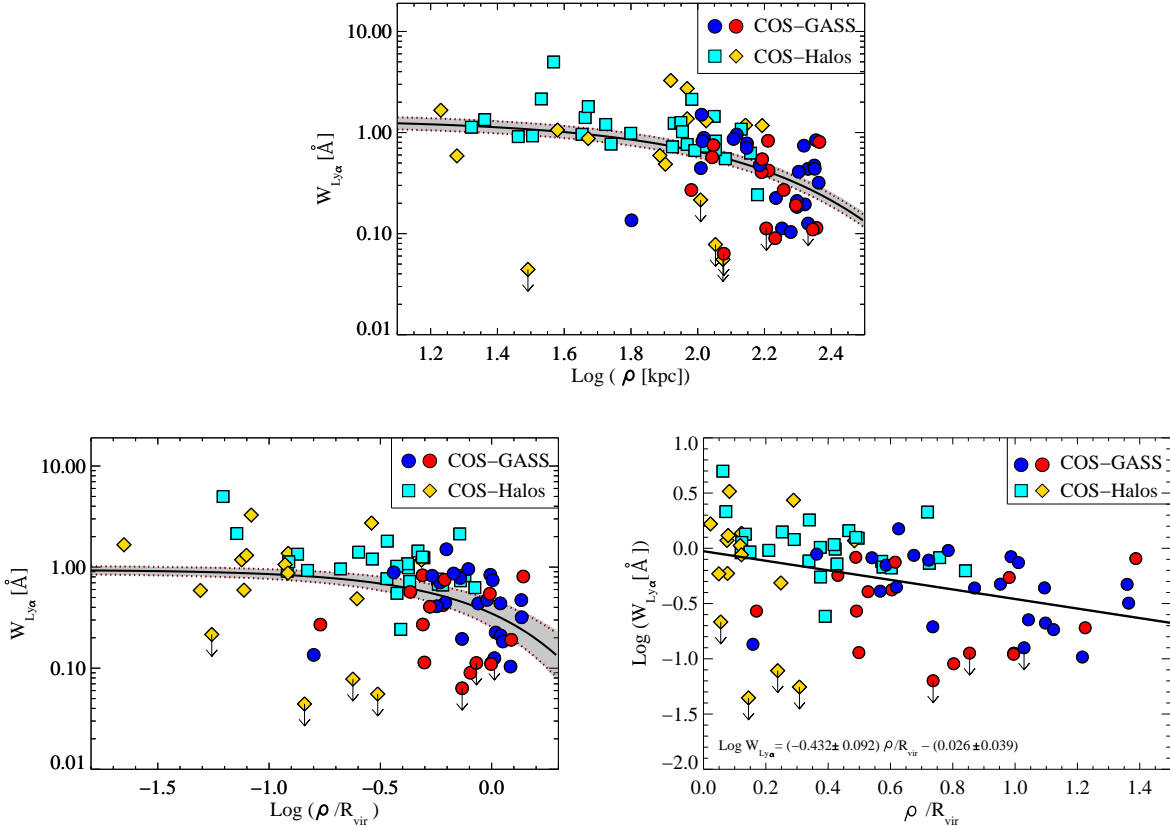


FIG. 2.— Top: Variation of Ly $\alpha$  equivalent widths as a function of impact parameter i.e.  $\rho$ . The COS-GASS data are shown as circles and the COS-Halos data are shown as diamonds. The galaxies are divided into two bins based on their specific star-formation rates (see text for details). This is indicated by the color of the symbols. Blue and cyan indicate blue star-forming galaxies from the COS-GASS and COS-Halos samples respectively. Red and yellow indicate the red passive galaxies. As shown with the black line, the radial distribution of the Ly $\alpha$  equivalent width can be fit as exponential with an e-folding scale length of 136 kpc. The grey shaded region represents the uncertainty associated with the fit. Bottom: Variation of Ly $\alpha$  equivalent widths as a function of normalized impact parameter i.e.  $\rho/R_{\text{vir}}$ . The panel on the left presents data using a logarithmic radial scale where as the one on the right is a linear radial scale. The best-fit exponential distribution is illustrated with the black solid line. The uncertainty associated with the fit is shown in grey. The best-fit parameters are labeled at the bottom of the right panel and imply an e-folding scale length of  $1.0 R_{\text{vir}}$ .

outer region of the halo). In order to cover the full range in impact parameter more completely and with better statistics, we combine our sample with the COS-Halos sample (Tumlinson et al. 2013). The COS-Halos sample covers a similar range in stellar masses and virial radii as our COS-GASS sample. For consistency, we recalculated the halo masses and virial radii for the COS-Halos sample from their stellar masses using the prescription by Behroozi et al. (2010). Similar to our limiting values, we assign the non-detections in the COS-Halos sample a value equivalent to 3 times the root mean squared (rms) noise in the spectra. The only remaining difference that we do not correct for is the difference in redshift between the two samples of about  $\sim 0.1$ . The combined sample together covers a large range of impact parameters from 10-250 kpc. This corresponds to a range in normalized impact parameter ( $\rho/R_{\text{vir}}$ ) of 0.2-1.4. Thus, the combined sample fully samples the CGM of the galaxies as a function of normalized impact parameter.

We re-investigate the distribution of neutral hydrogen as traced by Ly $\alpha$  equivalent width as a function of impact parameter and the normalized impact parameter for our combined sample. Similar studies have been done in the past with different samples (Lanzetta et al. 1995;

Chen et al. 1998; Tripp et al. 1998; Chen et al. 2001; Bowen et al. 2002; Prochaska et al. 2011; Stocke et al. 2013b; Tumlinson et al. 2013; Liang & Chen 2014, and references therein), and the Ly $\alpha$  equivalent width was found to decrease with increasing impact parameter. Figure 2 shows the equivalent width of the Ly $\alpha$  absorption line as a function of impact parameter and normalized impact parameter ( $\rho/R_{\text{vir}}$ ) for this combined sample. The Ly $\alpha$  equivalent widths are plotted in logarithmic units to show the range of values detected. The COS-GASS sample is plotted as filled circles and the COS-Halos sample is plotted as diamonds. Blue and cyan represents galaxies that have specific star formation rates (sSFR) of higher than  $10^{-11} \text{ yr}^{-1}$ . These galaxies are also referred to as “blue” galaxies in the rest of the paper. In red and yellow, are galaxies from the combined sample that have sSFRs lower than that value. These galaxies are referred to as “red” galaxies hereafter. The color definition is adopted from Tumlinson et al. (2011b). However, the color assignments for the COS-GASS sample is also consistent with the more rigorous definition by Schiminovich et al. (2007, see their Fig 7). The COS-GASS sample on a plot similar to Fig 7 of Schiminovich et al. (2007) is shown in Figure 3. The pa-

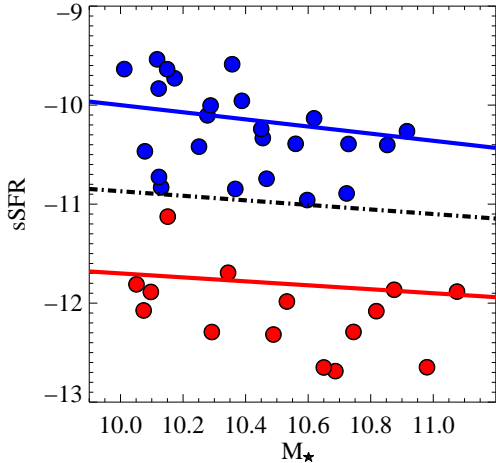


FIG. 3.— Galaxy color definition for the COS-GASS sample. The COS-GASS sample on the parameter space of stellar mass ( $M_*$ ) and sSFR. Based on the study by Schiminovich et al. (2007, see their Fig 7), we divide the parameter space into two-zones corresponding to red and blue galaxies. The galaxy grouping into the two colors following this definition is consistent with the color definition from Tumlinson et al. (2011b), which defines galaxies with sSFR higher than  $10^{-11} \text{ yr}^{-1}$  as blue and less than this value as red.

parameter space is divided half-way into red and blue galaxies. However, it is worth noting that galaxies closest to the dividing line are quite diverse and might correspond to a transitional phase (also known as “green valley”). For example, some of these galaxies show the Balmer series transition in emission as well as absorption. They also have a wide range of Ly $\alpha$  strength in their CGM. Unfortunately, our sample does not have a statistically significant number of such transitional phase galaxies so we can not probe the complexities of their CGM in detail.

The upper panel of Figure 2 shows that the equivalent widths of the Ly $\alpha$  absorbers start to drop off beyond an impact parameter of about 150 kpc. This same behavior is seen in the plot *vs.* normalized impact parameter (lower left panel). An alternative way to visualize the radial distribution of the Ly $\alpha$  absorbers is shown in the lower right panel, where the normalized impact parameter is plotted in linear units. A linear fit to the data in this plot yielded the following best-fit parameters

$$\text{Log}W_{\text{Ly}\alpha} = (-0.432 \pm 0.092) \frac{\rho}{R_{\text{vir}}} - (0.026 \pm 0.039) \quad (1)$$

This implies that the strength of Ly $\alpha$  data can be described as an exponential function of normalized impact parameter with an e-folding length of  $R_{\text{vir}}$  as follows:

$$W_{\text{Ly}\alpha} = 0.941 e^{-\rho/R_{\text{vir}}} \quad (2)$$

This same fit is shown in the lower left panel. A similar fit using the (un-normalized) impact parameters is shown in the top panel and yields a scale-length of 136 kpc.

We can also assess the velocity offsets between the Ly $\alpha$  absorbers and the systemic velocity of the central galaxy. Is this gas likely to be bound to the galaxy? We have therefore measured the displacement of the centroid of the Ly $\alpha$  absorption line from the galaxy’s systemic velocity. The systemic velocity is defined as the velocity corresponding to the SDSS-based redshift measurement

i.e.  $V_{\text{sys}} = cz$ , where  $c$  is the speed of light in vacuum. The uncertainty in systemic velocity is of the order  $\sim 30 \text{ km s}^{-1}$ .

Among the sightlines where Ly $\alpha$  was detected, 34/36 (94%) of the absorption features showed the centroid of the strongest component of the Ly $\alpha$  feature to be within  $250 \text{ km s}^{-1}$  of the galaxy’s systemic redshift. This suggests that the absorbers are most likely bound within the dark matter halo of the galaxy. To investigate this further, we estimate the escape velocity, for a parcel of gas located at the (1) distance of closest impact of the sightline ( $v_{\text{esc}}^{\rho}$ ) and (2) virial radius ( $v_{\text{esc}}^{\text{Rvir}}$ ). The values are presented in Table 2. These calculations were made assuming a spherically symmetric NFW profile (Navarro et al. 1996) for the dark matter halo with a concentration parameter of 15. Only 2/36 of Ly $\alpha$  absorbers have the velocity centroid of the strongest component larger than either of the escape velocities. This strongly suggests that the bulk of the Ly $\alpha$  absorbers are tracing the bound CGM. Similarly, if we consider all the components of the Ly $\alpha$  profiles, then the number of possibly escaping components increases to 5/48. In summary, 34/36 (94%) of the strongest Ly $\alpha$  components or 43/48 (90%) of all Ly $\alpha$  components have velocities smaller than escape velocity. Therefore, statistically the Ly $\alpha$  absorbers in our sample are likely to be probing the bound CGM.

We also find that the Ly $\alpha$  absorption-lines show velocities consistent with that of the velocity range observed in the 21cm line profiles of the H I gas within the galaxies. An example of the 21cm H I profiles of one of our galaxies (J1354+2433) is presented in the left panel of Figure 4. The Arecibo spectrum of the galaxy shows H I spread over a  $\approx \pm 200 \text{ km s}^{-1}$  (marked as the shaded region) in the rest frame of the galaxy. The rest-frame velocity was determined by subtracting the systemic velocity ( $v_{\text{sys}} = cz$ ) from the observed H I velocities. The velocity centroid of the Ly $\alpha$  absorption feature ( $v_{\text{Ly}\alpha}$ ) with respect to the systemic velocity of the host galaxy is marked as the red filled (strongest component) and open (weaker) components. The maximum velocity extent of the 21cm H I line profile in the same velocity end as the Ly $\alpha$  centroid is defined here as  $v_{\text{HI}}$ . The need to measure  $v_{\text{HI}}$  on either the redshifted or blueshifted side of the spectra based on the location of the Ly $\alpha$  centroid arises due to the fact that 21 cm H I profiles may be asymmetric with respect to the systemic velocity. For instance, if the Ly $\alpha$  centroid is blueshifted in the rest-frame of the galaxy, then we measure  $v_{\text{HI}}$  as the maximum velocity of the 21cm H I profile at zero flux blueward of the rest-frame. Hence, the estimates of the velocity offsets of the ISM and the CGM at the rest-frame are not impacted by the asymmetries in the 21cm H I profile.

The right panel of Figure 4 shows the rest-frame velocity distribution of the Ly $\alpha$  absorbers as a function of velocity distribution of 21cm H I profiles that traces the ISM of the host galaxies. In this figure, the centroids of the Ly $\alpha$  absorption features are marked with circles and the full range of velocity for the absorption features are shown as vertical bars. The centroid of the strongest component is shown as filled circle and the weaker components, if present, are shown as open circles. The color of the symbol represents the color of the galaxy as summarized in Table 1. The velocities are normalized to the

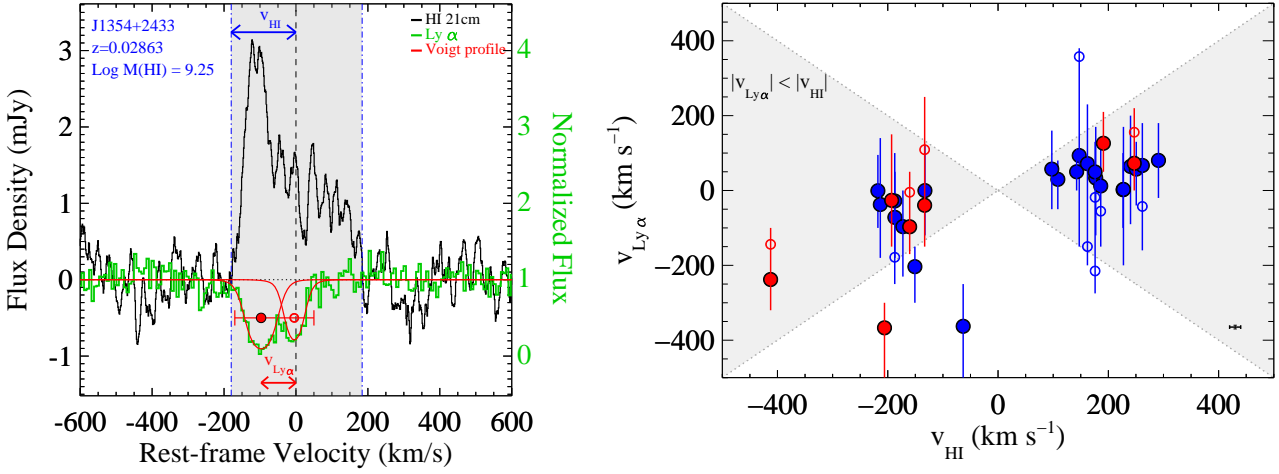


FIG. 4.— Left: 21 cm HI spectra of one of our target galaxies ( $M_{\text{HI}} = 1.8 \times 10^9 M_{\odot}$ ,  $\rho = 155$  kpc) from the GASS sample. This illustrates a typical HI profile for our sample. The abscissa and ordinate show the velocity in the rest-frame of the galaxy (based on SDSS emission-line estimation) and the flux in the 21 cm HI hyperfine transition respectively. The part of the spectrum showing the emission (observed, uncorrected for instrumental broadening) is indicated with the grey shaded region ( $\square$ ). The spectrum is smoothed to 20 km/s, and hence its resolution. The normalized Ly $\alpha$  profile for the galaxy is shown in green. The velocity centroid of the strongest component of the Ly $\alpha$  profile is shown as the filled red circle and that of the weaker component is shown as red open circle. The entire width of the Ly $\alpha$  profile is shown as the red line passing through the circles representing the centroids. The velocity offset of the centroid of the primary Ly $\alpha$  component from the systemic velocity (at 0 km s $^{-1}$  in the plot) is termed as  $v_{\text{Ly}\alpha}$ . We compare this with the velocity extent (half) of the HI profile,  $v_{\text{HI}}$ , again with respect to the systemic velocity of the galaxy, towards same velocity direction as the  $v_{\text{Ly}\alpha}$ . For example, if  $v_{\text{Ly}\alpha} > 0$ , then we define  $v_{\text{HI}}$  as the velocity extent of the 21 cm HI profile towards the positive velocity wing of the profile. For the case shown above,  $v_{\text{HI}}$  is defined on the negative velocity wing of the HI profile and is marked on the plot as the blue double headed arrow. Choosing the right velocity edge of the 21 cm HI profile to compare with the offset of the Ly $\alpha$  centroid from the systemic velocity reduces the effect of asymmetries on the HI profile in the analysis. For symmetric 21 cm HI profiles,  $v_{\text{HI}}$  is simply the velocity half width of the profile. Right: The offset of the velocity centroid of Ly $\alpha$  absorbers  $v_{\text{Ly}\alpha}$  as a function of the velocity (half) widths,  $v_{\text{HI}}$ , of the 21 cm HI profiles. The velocities are measured with respect to the systemic velocity of the host galaxies based on the redshift measurements from optical emission lines. The HI velocity widths are corrected for instrumental broadening. The centroid of the strongest component is shown as a filled circle and those of weaker components are shown as open circles. The full widths of the Ly $\alpha$  features are shown as the vertical bars passing the centroids. The color of each circle indicates the color of the galaxy. The shaded grey region indicates the parameter space where the Ly $\alpha$  centroids lie within the HI extent of the galaxies. The uncertainties in the velocity measurements are shown in the right hand corner.

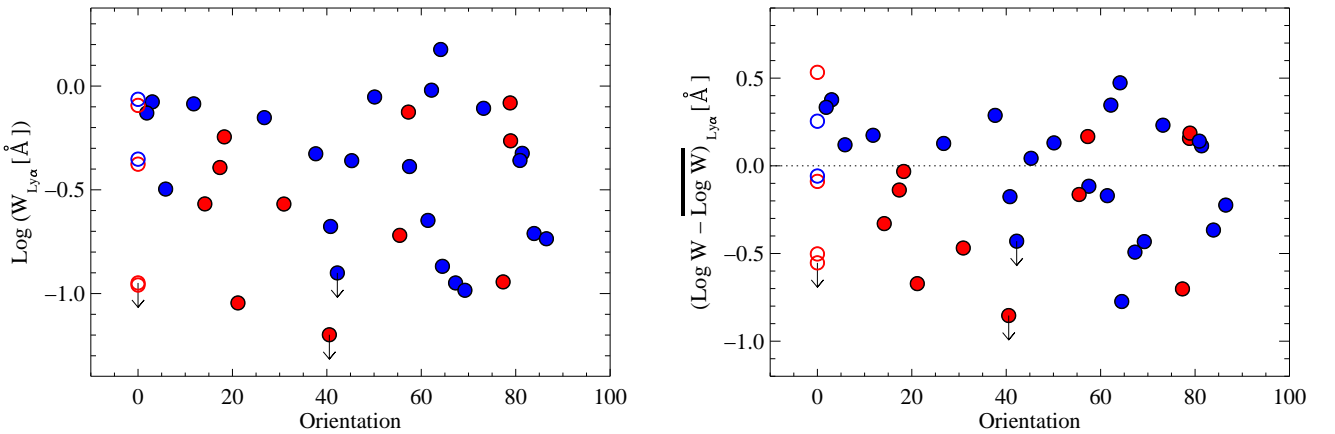


FIG. 5.— Left: Ly $\alpha$  equivalent width as a function of orientation of the QSO sightline with respect to the optical major axis of the galaxy. The open circles represent galaxies that are face-on and their orientation parameter is set to zero. The color of the circles represents the color of the galaxy that is summarized in Table 1. Right: The excess in Ly $\alpha$  equivalent width ( $[\text{Log } W - \overline{\text{Log } W}]_{\text{Ly}\alpha}$ ), which is independent of the impact parameter of the sightlines, as a function of orientation of the QSO sightlines with respect to the target galaxy. The dotted line corresponds to the expected equivalent width based on fit to Figure 2. We find no correlations between orientation and Ly $\alpha$  strengths. The face-on galaxies are excluded while measuring the strength of the correlation.

rest-frame using optical redshifts from the SDSS.

The grey shaded area represents the region of the space where  $|\delta V_{\text{Ly}\alpha}| \leq |\delta V_{\text{HI}}|$ . 90% (26/29) of the centroids of the strongest Ly $\alpha$  absorbers lie within the velocity range of the 21 cm H I emission-line associated with the target galaxy. Two notable exceptions are the blue galaxy J1541+2817 and the red galaxy J1515+0701. The H I spectral range in J1541+2817 extends from  $-73$  to  $107 \text{ km s}^{-1}$  and the Ly $\alpha$  absorber was detected at  $-399 \text{ km s}^{-1}$ . Similarly, the Ly $\alpha$  velocity centroid of J1515+0701 is  $-362 \text{ km s}^{-1}$  whereas the H I associated with the galaxy spans a range of  $-207$  to  $303 \text{ km s}^{-1}$  with respect to the systemic velocity of the galaxy. The origin of the offsets in these two systems is not clear (they do not seem to be in unusual environments relative to the other systems). For most galaxies, that is 20/29 (>66%), the entire Ly $\alpha$  profile lies within the 21cm H I profile. Therefore, we conclude that the vast majority of the absorbing systems are very likely to be gravitationally bound material inside the dark matter halo.

Next we have looked for any dependence in the properties of absorbers on the orientation of the sightline with respect to the major axis of the galaxy. This would potentially allow us to distinguish between Ly $\alpha$  arising in an extended disk, in bipolar outflows, or in material simply tracing the dark matter halo. Figure 5 presents the strength of Ly $\alpha$  equivalent width as a function of orientation of the sightline with respect to the galaxy (e.g. Kacprzak et al. 2010; Bordoloi et al. 2011). No correlation has been observed. Since we showed previously that Ly $\alpha$  equivalent widths correlate with the normalized impact parameters, we corrected for any impact parameter dependence by dividing the observed Ly $\alpha$  equivalent width by the average Ly $\alpha$  equivalent width at that impact parameter (described by the best-fit line of Equation 1). We refer to this term as the impact parameter corrected excess in equivalent width, or simply as the excess equivalent width. Here again, we see that the excess in the Ly $\alpha$  equivalent width does not correlate with orientation of the sightline with respect to the major axis of the target galaxy for the full sample. Part of the reason for the non-existence of any correlation could be because we are probing mostly the outer CGM.

*Therefore, we conclude that the Ly $\alpha$  absorbers we are studying trace a roughly spherical distribution of gravitationally-bound gas with a characteristic size comparable to the virial radius. This is what we would expect for the CGM.*

### 3.2. Correlation between properties of the CGM and the ISM

We now explore the connection between the gas in the CGM as traced by the Ly $\alpha$  absorbers and the cool neutral ISM as traced by the HI 21cm line. Figure 6 shows the results for the COS-GASS sample. The abscissa indicates their 21 cm H I mass on the bottom and their estimated H I radii on the top. The radius of the disk,  $R_{\text{HI}}^2$ , was indirectly estimated using the extremely tight relationship between H I mass and size as observed by Swaters et al. (2002). We find a positive correlation between the equivalent width of Ly $\alpha$  absorbers in the CGM

<sup>2</sup>  $R_{\text{HI}}$  is defined as the annuli of H I mass density of  $1 M_{\odot} \text{ pc}^{-2}$  or column density  $1.3 \times 10^{20} \text{ cm}^{-2}$ .

and M(HI). A Kendall  $\tau$  (Brown et al. 1974) test implies that the null hypothesis of no correlation can be rejected at the 98.5% confidence level<sup>4</sup>. This also implies a positive correlation between the equivalent width of Ly $\alpha$  and the size of the H I disk. We find even stronger correlations between the suitably normalized quantities<sup>3</sup>. This is shown in the right panel where the excess Ly $\alpha$  equivalent width is plotted as a function of H I mass fraction (M(HI)/ $M_{\star}$ ) of the host galaxy. The resulting correlation is inconsistent with the null hypothesis at the 99.8% confidence level<sup>4</sup>. At the same time, we do not find any correlation between the Ly $\alpha$  equivalent width and the stellar mass of the galaxies.

To visualize our data and to help in its interpretation, we also performed a stacking experiment to study the average properties of the CGM as a function of 21 cm H I mass within their host galaxies. We divided our sample into four sub-samples based on their H I masses. Spectra of each sub-sample were stacked within  $\pm 1500 \text{ km s}^{-1}$  of the rest-frame Ly $\alpha$  transition associated with the target galaxy. Each spectrum was centered at the centroid of the Ly $\alpha$  absorption feature before the stacking was performed. For the three non-detections, we used the systemic velocity of the target galaxies as zero velocity. The results are presented in Figure 7. Each of these stacks comprise approximately 8-10 spectra.

We detected Ly $\alpha$  absorption-lines in each stack. However, their strength shows considerable variations. The Ly $\alpha$  strengths increased monotonically with increasing H I mass within the galaxy. Both the peak depth of the absorption features as well as equivalent widths of the absorption features increase with increasing H I mass. Since most of the individual Ly $\alpha$  absorption-lines are saturated, the behavior of the stacks is indicative of the increase in the covering fraction of Ly $\alpha$  in the CGM of galaxies as a function of increasing H I mass. A similar trend is also seen as a function of H I fraction (M(HI)/ $M_{\star}$ ). Another way to illustrate the same conclusion is to note the fractional increase in saturated Ly $\alpha$  lines as a function of H I mass. For example, for galaxies with M(HI)  $< 10^{9.1} M_{\odot}$  the fraction of Ly $\alpha$  absorbers with  $W_{\text{Ly}\alpha} > 0.3 \text{ \AA}$  is about 30%. It increases to  $\sim 55\%$  and  $67\%$  for galaxies with M(HI) between  $10^{9.1-9.45} M_{\odot}$  and M(HI) between  $10^{9.45-9.9} M_{\odot}$  respectively. It reaches 100% in the sub-sample with M(HI)  $> 10^{9.9} M_{\odot}$ .

We also investigated the combined influence of impact parameter and H I mass on the equivalent width of the Ly $\alpha$  profile. To do so, we divided the sample into 2 impact parameter bins - one lower and the other higher than 170 kpc. We then sub-divided each sub-sample into galaxies with H I mass less or greater than 9.45 dex. The left panel of Figure 8 shows the stacked spectra for each

<sup>3</sup> We are using  $M_{\star}$  as a proxy for halo mass. The normalization by the two kinds of masses yield very similar results as  $M_{\text{halo}}$  is derived from  $M_{\star}$ .

<sup>4</sup> The test was performed on our censored data using the astronomy survival analysis code ASURV (Feigelson & Nelson 1985). ASURV is capable of handling single and doubly censored data. Accuracy of these probabilities can be affected by larger number of censored values and other conditions. Since less than a quarter of our sample has censored values, we do not expect substantial inaccuracies. However, caution is appropriate as is for results from Kendall's test on any sample (Wang & Wells 2000).

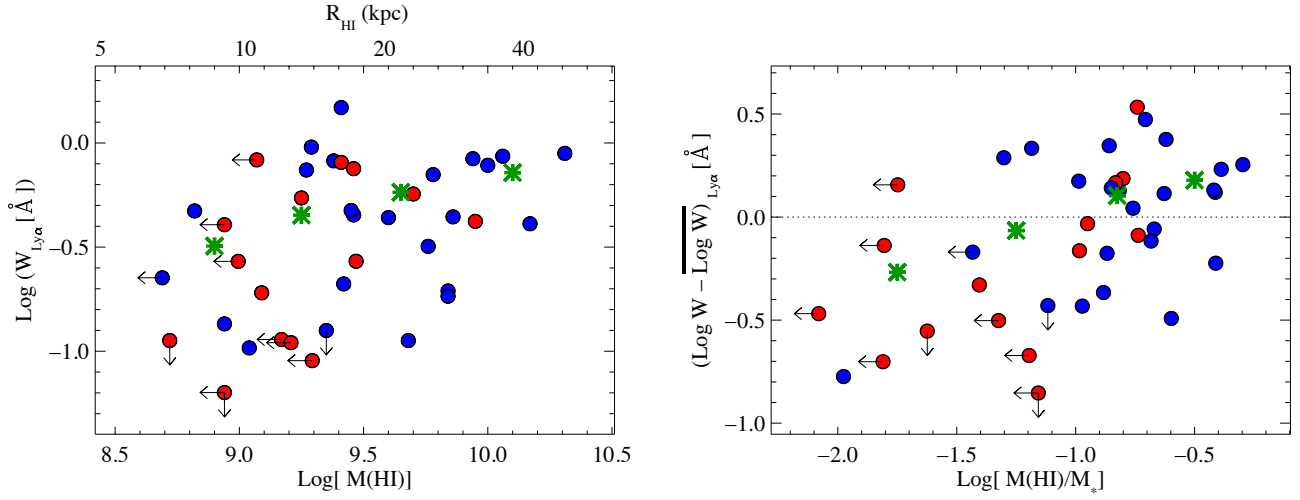


FIG. 6.— Equivalent width of Ly $\alpha$  as a function of 21 cm HI mass and the excess in Ly $\alpha$  equivalent width ( $[\text{Log } W - \overline{\text{Log } W}]_{\text{Ly}\alpha}$ ), which is independent of impact parameter of the sightline, as a function of the HI mass fraction  $M_{\text{HI}}/M_*$  of the galaxies. The size of the HI disk is indirectly estimated from the tight HI size-mass relation (Swaters et al. 2002). We find statistically significant correlations with a statistical significance of 98.5% for the left panel and 99.8% for the right. The top x-axis of the left panel converts the HI mass to a radius of the HI disk (see text for details). The average equivalent widths derived from the stacked spectra (presented in the next figure) are plotted as green asterisk in the left panel. The averages derived from the data points in the right panel are shown as green asterisk.

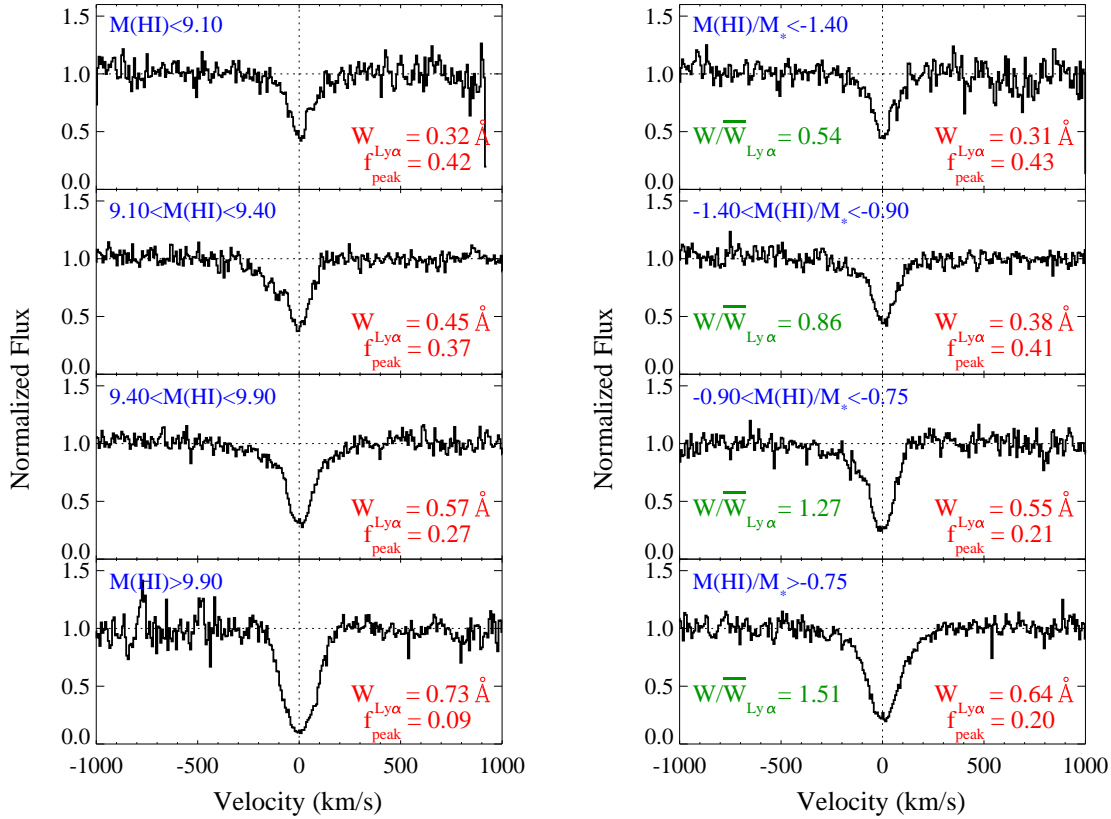


FIG. 7.— Composite Ly $\alpha$  absorption-lines stacked as a function of HI mass and gas fraction ( $M_{\text{HI}}/M_*$ ). Individual Ly $\alpha$  absorbers were centered at their centroid of the feature i.e.  $v_{\text{centroid}} = 0 \text{ km s}^{-1}$ , and then added to produce the stacks. Each of the stacked spectra are composed of approximately 8-10 individual spectra in that labeled HI mass range. The equivalent width and the peak depth ( $f_{\text{peak}}$ ) of the absorption features are labeled in the right corner of each plot in red. The average values of the excess in Ly $\alpha$  equivalent width for the sightlines used in creating the stacks are printed in green. These set of stacks are not corrected for impact parameter variations and consequently show a weaker trend just like the left panel of Figure 5. Similar plots with impact parameter bins are presented in the next figure.

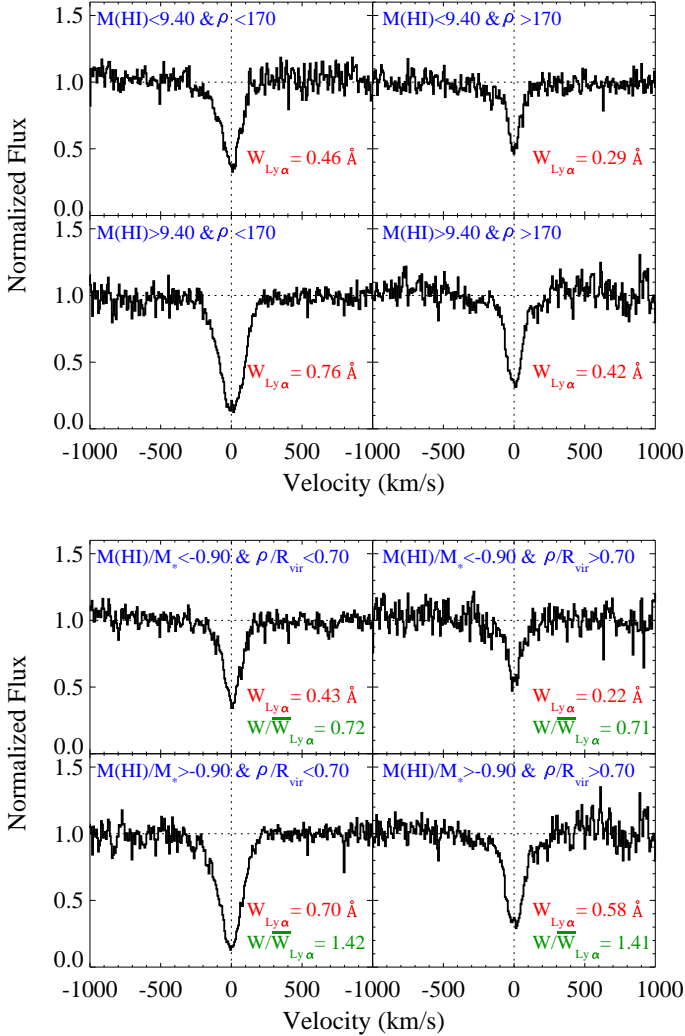


FIG. 8.— Top: Stacks of Ly $\alpha$  absorption similar to those presented in Figure 7 but with bins that divide the sample into subsets of impact parameter - one less than and the other greater than 170 kpc. The values for the bins were chosen such that the sample is divided more or less equally into 4 bins. Systematic variations the strength of the Ly $\alpha$  absorption as a function of HI mass within each bin can be seen. The equivalent width of the features are labeled in the right corner of each plot in red. Bottom: Stacks similar to those on the top, but binned by HI mass fraction and normalized impact parameter ( $\rho/R_{\text{vir}}$ ). The sample was divided along the median value of normalized impact parameter of 0.70. The average values of the excess in Ly $\alpha$  equivalent width for the sightlines that go into the stacks are printed in green. As expected, these are independent of the normalized impact parameter bins.

of the bins. This verifies the influence of H I mass as well as impact parameter separately on the strength of Ly $\alpha$  profiles. A similar set of stacks were produced for the hybrid parameters -  $M(\text{HI})/M_*$  and  $\rho/R_{\text{vir}}$  - these further confirm the correlation between  $M(\text{HI})/M_*$  and the strength of the Ly $\alpha$  absorption lines.

We also explore the effect of the size of the H I disk on the properties of the Ly $\alpha$  absorbers. Figure 9 plots the equivalent widths of the Ly $\alpha$  absorbers as a function of the impact parameter normalized by the HI radius (i.e.  $\rho/R_{\text{HI}}$ ). Sightlines probing the CGM within  $\sim 7 R_{\text{HI}}$  all show strong saturated Ly $\alpha$  absorption features ( $W_{\text{Ly}\alpha} > 0.4 \text{ \AA}$ ). The other striking feature of the plot is the step drop in the strength of the absorption-

lines at larger normalized radii.

*In conclusion, there is a significant correlation between the strength of the Ly $\alpha$  absorption-lines tracing the CGM and the mass and by extension the extent of the distribution of 21 cm H I component of the galaxy disk.*

### 3.3. Relationships of the CGM to the H I and Star Formation

While the properties of the CGM traced by Ly $\alpha$  correlate with the H I properties of the host galaxy, the H I properties also correlate with the star formation rates of the galaxies (Schiminovich et al. 2010; Catinella et al. 2010). In this subsection we examine the correlations between these parameters in an attempt to isolate the primary physical correlations. This can be addressed most easily by determining if there is a correlation between the Ly $\alpha$  equivalent width and the star-formation rate, and then comparing this to the strength of the correlation between Ly $\alpha$  equivalent width and H I mass. This will help us probe the physics behind the correlations and isolate the driving mechanisms that connect gas at distances of hundreds of kpc to the central galaxy.

We therefore repeat the same exercise for the SFR as was done for the H I masses in Figure 6. The corresponding plots showing the distribution of Ly $\alpha$  equivalent width as a function of SFR and the excess in Ly $\alpha$  equivalent width as a function of specific SFR (sSFR =  $\text{SFR}/M_*$ ) are presented in Figure 10. The Kendall's rank correlation test reveals that the probability of the null hypothesis of no correlation between Ly $\alpha$  equivalent width and SFR can only be excluded at the 89.9% confidence level, while the corresponding probability for the correlation between excess Ly $\alpha$  equivalent width and sSFR is 97.5%. Comparing these results to the results in Figure 6 implies that *the CGM properties correlate better with the properties of the atomic gas than those of the current star formation.*

This result may not be surprising. Warm ionized gas accreted from the CGM has to pass through the atomic phase (traced by H I 21cm) before condensing into molecular phase, which can then facilitate star formation. The various processes that connect gas inflow to star-formation add intrinsic scatter and therefore, weaken the correlation. For example, the efficiency of the conversion of gas from the atomic to molecular phase, and of molecular gas into stars, may show substantial variation among and within galaxies. The dispersion in the correlation between Ly $\alpha$  equivalent width in the CGM and the SFRs within the galaxies may indicate lags in the multi-step process of accretion of warm gas via the CGM, condensation to atomic gas, conversion to molecular gas, and finally star-formation.

Nevertheless, we do find a significant difference in the Ly $\alpha$  equivalent width distribution between red and blue galaxies. The blue galaxies show a uniform Ly $\alpha$  strength profile as a function of impact parameter whereas the red galaxies show a much larger dispersion at all impact parameters including small  $\rho/R_{\text{vir}}$  (Figure 2). We do find red galaxies with strong Ly $\alpha$  profiles (similar to that found by Thom et al. 2012), but almost half of the red galaxies either show weak Ly $\alpha$  or even no Ly $\alpha$  at our detection limit. To further probe the relationship between the CGM and star-formation, a paper detailing the analysis of the properties of neutral hydrogen and metal lines

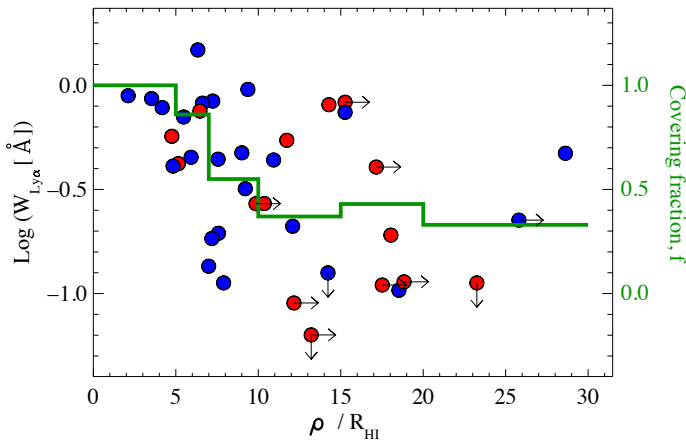


FIG. 9.— Ly $\alpha$  equivalent width as a function of the impact parameter normalized by the radius of the H I disk ( $\rho/R_{\text{HI}}$ ). The absorbers are shown as colored filled circles with their colors indicating the color of the galaxy as defined by their sSFR and presented in Table 1. Sightlines within about  $7 R_{\text{HI}}$  all produce strong saturated Ly $\alpha$  lines. In green we plot the covering fraction of strong Ly $\alpha$  absorbers with equivalent width larger than  $0.32 \text{ \AA}$  ( $-0.5$  dex). This corresponds to a column density of  $\approx 6 \times 10^{13} \text{ cm}^{-2}$  or larger. The right ordinate is labeled to indicate the scale.

from the combined COS-Halos and COS-GASS surveys is in preparation.

#### 4. SUMMARY & IMPLICATIONS

The CGM of galaxies acts as the pathway for baryons and energy to get in and out of the galaxies. The properties of the gas in the CGM not only hold clues to the evolutionary history of the galaxy but also will influence the evolution of the galaxy in the future. After gas from the CGM is accreted onto the galaxy, it is expected to first pass through a phase as atomic hydrogen located primarily in the outer disk.

Therefore, in order to explore the connection between the CGM and the atomic gas reservoir in galactic disks, we have undertaken an observational program with the COS aboard the HST. This program probed the CGM of 45 galaxies out to an impact parameter of  $\approx 250$  kpc at the rest-frame of the galaxies. The sample covers galaxies in the stellar mass ranges of  $10^{10.1-11.1} M_{\odot}$ , and as such, was designed to probe galaxies spanning the stellar mass range where galaxy the galaxy population transitions from lower mass star-forming galaxies that are rich in cold interstellar gas to more massive quiescent galaxies that contain relatively little cold interstellar gas.

Our sample was chosen from the GASS project, which provided Arecibo H I spectra, GALEX photometry, SDSS photometry and spectroscopy and all other related data products. For 5 of the galaxies in the sample that did not have GASS H I spectra, we obtained H I spectral measurements with the GBT.

The COS-GASS sample allowed us to study for the first time the connection between the CGM and the ISM of galaxies. Based on the analysis presented in this paper, we found the following:

1. We detected Ly $\alpha$  absorption in 92% (36/39) of the target galaxies for which we have useful data at the expected position of the Ly $\alpha$  transition. Of these detections, 94% (34/36) show Ly $\alpha$  absorption

within  $\pm 250 \text{ km s}^{-1}$  of the systemic velocity of their host galaxy.

2. Combining our sample with the complementary COS Halos sample, we found that the radial distribution of Ly $\alpha$  equivalent widths can be fit as an exponential function with an e-folding scale-length of  $R_{\text{vir}}$ . We defined an excess equivalent width for each Ly $\alpha$  absorption line with respect to the best-fit radial distribution.
3. The equivalent widths of the Ly $\alpha$  absorbers do not correlate with orientation of the sightline with respect to the optical major axis of the target galaxy.
4. These three results imply that Ly $\alpha$  absorbers are tracing a roughly spherical distribution of gravitationally-bound gas with a characteristic size similar to the virial radius of the dark matter halo. This can indeed be described as a Circum-Galactic Medium.
5. We find positive correlations (at a confidence of 98.5%) between the equivalent width of Ly $\alpha$  and  $M_{\text{HI}}$ . An even stronger correlation (at a confidence level of 99.8%) is present between the excess (impact-parameter-corrected) Ly $\alpha$  equivalent width ( $[\text{Log } W - \overline{\text{Log } W}]_{\text{Ly}\alpha}$ ) and the H I mass fraction ( $M_{\text{HI}}/M_{\star}$ ).
6. Similar correlations were also seen in Ly $\alpha$  spectra stacked as a function of H I mass and mass fraction. The underlying reason for the observed increase in Ly $\alpha$  absorption strength in the stacks with H I mass and mass fraction is due to the increase in the covering fraction of optically-thick neutral gas. For example, the covering fraction of Ly $\alpha$  absorption is almost 100% in the sub-sample with H I mass,  $M(\text{HI}) > 10^{9.9} M_{\odot}$ . This correlation was observed for sightlines probing both smaller as well as larger impact parameters and is independent of the correlation between the equivalent width of Ly $\alpha$  and impact parameter.
7. We have used the HI masses to estimate the radii of the HI disks. We then found that the equivalent width of the Ly $\alpha$  line decreases as the ratio of  $\rho/R_{\text{HI}}$  increases. Sightlines probing the gas within  $\sim 7 R_{\text{HI}}$  all show strong Ly $\alpha$  absorption features (equivalent widths  $> 0.4 \text{ \AA}$ ).
8. The strength of the Ly $\alpha$  absorption is also correlated with the SFR in their host galaxies. However, we find the correlations between the equivalent width of Ly $\alpha$  and H I mass and between excess Ly $\alpha$  equivalent width and HI mass fraction to be stronger than the corresponding correlations with SFR and  $\text{SFR}/M_{\star}$ .

These results are consistent with a picture in which the reservoir of cold gas in galaxies is fed by accretion of gas through/from the CGM. In particular, a process that removes or diminishes this CGM reservoir would lead to a subsequent drop in the cold gas content of the galaxy and hence to a diminished star formation rate.

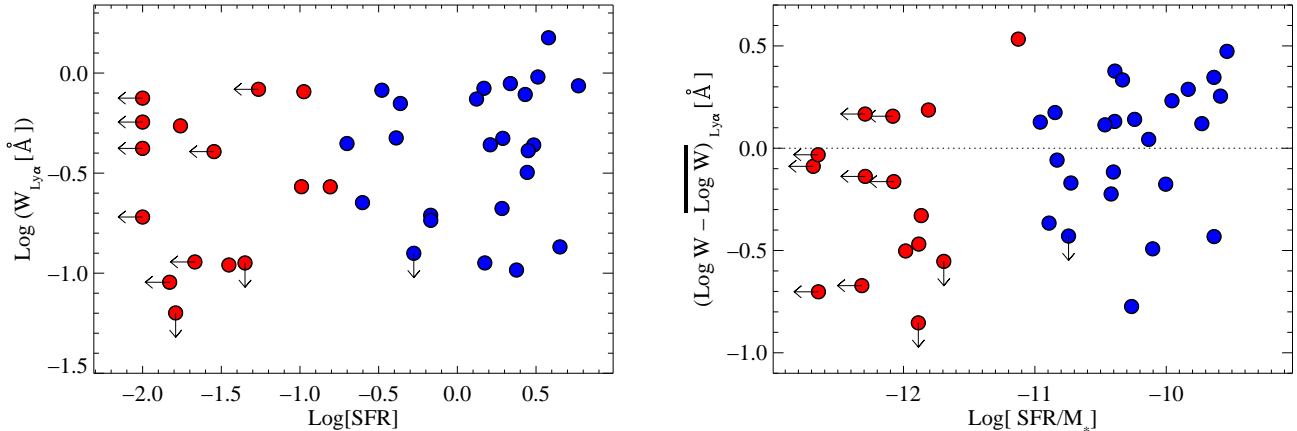


FIG. 10.— Left: Variation in the Ly $\alpha$  equivalent width as a function of SFR. The absorbers are shown as colored filled circles with their colors indicating the color of the galaxy as defined by their sSFR and presented in Table 1. Right: The excess Ly $\alpha$  equivalent width as a function of specific SFR. The correlations have a statistical significance of only 89.9% (left panel) and 97.5% (right panel). These are weaker than the corresponding ones in Figure 5.

The results above are suggestive of a gas accretion history that is more or less gradual and continuous, at least among the HI-rich galaxies. For a highly episodic process we would expect to find only a weak or no correlation between the CGM and the cold gas content of galaxies. A picture of continuous gas accretion is also consistent with the result that material producing strong (optically-thick) Ly $\alpha$  absorption-lines has a near-unit covering factor in the CGM of the HI-rich star-forming galaxies in our sample. Interestingly, the HI-poor quiescent galaxies show a wider range in the strength of their Ly $\alpha$  absorption features. Many are weak or even non-detections, but we do detect relatively strong absorption feature in others. This might indicate a more sporadic accretion history for them.

It is noteworthy that the properties of the CGM traced by Ly $\alpha$  absorption are more closely correlated with the properties of HI than with the properties of the star formation. This may be explained by the fact that the H I is mostly in the outer disk and should be more directly related to the effects of accretion from the CGM. In addition, this stronger connection suggests that the material probed with Ly $\alpha$  absorption is primarily gas flowing from the CGM to the galaxy, rather than out-flowing gas driven by feedback provided by the ongoing star-formation. This is further supported by the uniformity in the distribution of the Ly $\alpha$  absorbers with respect to the galaxy major/minor axis, and the consistency between the velocity spread of the Ly $\alpha$  absorbers and the 21 cm H I in the galaxy disk.

Having established a connection between the cool gas in the CGM and the HI in the galactic disk, it will be important to further probe the interface region between the outer disk and the inner CGM to look for clues as to how and where the accretion/condensation is happening.

We thank the HST and GBT staff for support during the observations. We also thank Cameron Hummels, Jessica Werk, Xavier Prochaska, Hsiao-Wen Chen, for useful discussions. This work is based on observations with the NASA/ESA Hubble Space Telescope, which is operated by the Association of Universities for Research in Astronomy, Inc., under NASA contract NAS5-26555. SB and TH were supported by grant HST GO 12603. BC is the recipient of an Australian Research Council Future Fellowship (FT120100660).

This project also made use of SDSS data. Funding for SDSS-III has been provided by the Alfred P. Sloan Foundation, the Participating Institutions, the National Science Foundation, and the U.S. Department of Energy Office of Science. The SDSS-III web site is <http://www.sdss3.org/>.

SDSS-III is managed by the Astrophysical Research Consortium for the Participating Institutions of the SDSS-III Collaboration including the University of Arizona, the Brazilian Participation Group, Brookhaven National Laboratory, Carnegie Mellon University, University of Florida, the French Participation Group, the German Participation Group, Harvard University, the Instituto de Astrofísica de Canarias, the Michigan State/Notre Dame/JINA Participation Group, Johns Hopkins University, Lawrence Berkeley National Laboratory, Max Planck Institute for Astrophysics, Max Planck Institute for Extraterrestrial Physics, New Mexico State University, New York University, Ohio State University, Pennsylvania State University, University of Portsmouth, Princeton University, the Spanish Participation Group, University of Tokyo, University of Utah, Vanderbilt University, University of Virginia, University of Washington, and Yale University.

*Facilities:* Sloan () COS () GBT ()

#### REFERENCES

- Baldry, I. K., Glazebrook, K., Brinkmann, J., et al. 2004, *ApJ*, 600, 681  
 Behroozi, P. S., Conroy, C., & Wechsler, R. H. 2010, *ApJ*, 717, 379  
 Blanton, M. R., Hogg, D. W., Bahcall, N. A., et al. 2003, *ApJ*, 592, 819  
 Bordoloi, R., Lilly, S. J., Knobel, C., et al. 2011, *ApJ*, 743, 10  
 Bordoloi, R., Tumlinson, J., Werk, J. K., et al. 2014, *ApJ*, 796, 136  
 Borthakur, S., Heckman, T., Strickland, D., Wild, V., & Schiminovich, D. 2013, *ApJ*, 768, 18  
 Bowen, D. V., Pettini, M., & Blades, J. C. 2002, *ApJ*, 580, 169  
 Brown, B. W., Hollander, M., & Korwar, R. M. 1974, *Reliability and Biometry*, 327, 354  
 Catinella, B., Schiminovich, D., Kauffmann, G., et al. 2010, *MNRAS*, 403, 683

- . 2012, *A&A*, 544, A65
- Catinella, B., Schiminovich, D., Cortese, L., et al. 2013, *MNRAS*, 436, 34
- Chen, H.-W., Lanzetta, K. M., Webb, J. K., & Barcons, X. 1998, *ApJ*, 498, 77
- . 2001, *ApJ*, 559, 654
- Dekel, A., Birnboim, Y., Engel, G., et al. 2009, *Nature*, 457, 451
- Eisenstein, D. J., Weinberg, D. H., Agol, E., et al. 2011, *AJ*, 142, 72
- Elbaz, D., Dickinson, M., Hwang, H. S., et al. 2011, *A&A*, 533, A119
- Feigelson, E. D., & Nelson, P. I. 1985, *ApJ*, 293, 192
- Haynes, M. P., Giovanelli, R., Martin, A. M., et al. 2011, *AJ*, 142, 170
- Johnson, S. D., Chen, H.-W., & Mulchaey, J. S. 2015, *ArXiv e-prints*
- Kacprzak, G. G., Churchill, C. W., Ceverino, D., et al. 2010, *ApJ*, 711, 533
- Kauffmann, G., Heckman, T. M., White, S. D. M., et al. 2003, *MNRAS*, 341, 33
- Kereš, D., Katz, N., Fardal, M., Davé, R., & Weinberg, D. H. 2009, *MNRAS*, 395, 160
- Kereš, D., Katz, N., Weinberg, D. H., & Davé, R. 2005, *MNRAS*, 363, 2
- Lanzetta, K. M., Bowen, D. V., Tytler, D., & Webb, J. K. 1995, *ApJ*, 442, 538
- Liang, C. J., & Chen, H.-W. 2014, *MNRAS*, 445, 2061
- Lilly, S. J., Carollo, C. M., Pipino, A., Renzini, A., & Peng, Y. 2013, *ApJ*, 772, 119
- Moran, S. M., Heckman, T. M., Kauffmann, G., et al. 2012, *ApJ*, 745, 66
- Navarro, J. F., Frenk, C. S., & White, S. D. M. 1996, *ApJ*, 462, 563
- Prochaska, J. X., Weiner, B., Chen, H.-W., Mulchaey, J., & Cooksey, K. 2011, *ApJ*, 740, 91
- Saintonge, A., Kauffmann, G., Kramer, C., et al. 2011, *MNRAS*, 415, 32
- Schiminovich, D., Wyder, T. K., Martin, D. C., et al. 2007, *ApJS*, 173, 315
- Schiminovich, D., Catinella, B., Kauffmann, G., et al. 2010, *MNRAS*, 408, 919
- Shull, J. M. 2014, *ApJ*, 784, 142
- Springob, C. M., Haynes, M. P., Giovanelli, R., & Kent, B. R. 2005, *ApJS*, 160, 149
- Stocke, J. T., Keeney, B. A., Danforth, C. W., et al. 2013a, *ApJ*, 763, 148
- . 2013b, *ApJ*, 763, 148
- Swaters, R. A., van Albada, T. S., van der Hulst, J. M., & Sancisi, R. 2002, *A&A*, 390, 829
- Thom, C., Tumlinson, J., Werk, J. K., et al. 2012, *ApJ*, 758, L41
- Tripp, T. M., Lu, L., & Savage, B. D. 1998, *ApJ*, 508, 200
- Tripp, T. M., Meiring, J. D., Prochaska, J. X., et al. 2011, *Science*, 334, 952
- Tumlinson, J., Werk, J. K., Thom, C., et al. 2011a, *ApJ*, 733, 111
- Tumlinson, J., Thom, C., Werk, J. K., et al. 2011b, *Science*, 334, 948
- . 2013, *ApJ*, 777, 59
- Wang, W., & Wells, M. T. 2000, *Statistica Sinica*, 10, 1199
- Werk, J. K., Prochaska, J. X., Tumlinson, J., et al. 2014, *ApJ*, 792, 8
- Whitaker, K. E., van Dokkum, P. G., Brammer, G., et al. 2013, *ApJ*, 770, L39

TABLE 1  
DESCRIPTION OF GALAXY PROPERTIES.

Galaxy	GASS ID	RA	Dec	z	$V_{\text{sys}}^{\text{a}}$ (km s $^{-1}$ )	$M_{\star}$ (Log $M_{\odot}$ )	$M_{\text{halo}}^{\text{b}}$ (Log $M_{\odot}$ )	$R_{\text{vir}}$ (kpc)	$M_{\text{HI}}$ (Log $M_{\odot}$ )	$\Delta V_{\text{HI}}^{\text{c}}$ (km s $^{-1}$ )	$R_{\text{HI}}^{\text{d}}$ (kpc)	Source (Survey)	sSFR $^{\text{e}}$ (Log yr $^{-1}$ )	Color $^{\text{f}}$
J0159+1346	3936	29.941	13.781	0.0441	13232	10.1	11.6	163	9.4	-126 – 147	16.2	GASS	-9.5	Blue
J0808+0512	19852	122.068	5.216	0.0308	9227	10.8	12.5	324	<8.9	–	8.4	GBT	-12.0	Red
J0852+0309	8096	133.229	3.152	0.0345	10351	10.3	11.8	179	9.7	-195 – 143	22.6	GASS	-10.1	Blue
J0908+3234	22391	137.232	32.576	0.0490	14677	10.5	12.0	212	<9.3	–	14.0	GBT	<-12.3	Red
J0914+0836	20042	138.684	8.601	0.0468	14039	10.0	11.6	156	9.0	-77 – 108	10.3	GASS	-9.6	Blue
J0930+2853	32907	142.538	28.898	0.0349	10462	10.5	11.9	208	9.4	-190 – 185	15.0	GASS	-10.7	Blue
J0931+2632	53269	142.817	26.550	0.0458	13718	11.0	13.0	454	<9.2	–	12.0	GASS	<-12.6	Red
J0936+3204	33214	144.101	32.079	0.0269	8073	10.3	11.8	187	8.7	-31 – 242	6.9	GASS	-11.7	Red
J0937+1658	55745	144.292	16.977	0.0278	8328	10.9	12.8	399	8.9	-151 – 157	9.1	GASS	-10.3	Blue
J0951+3537	22822	147.937	35.622	0.0270	8091	10.6	12.1	229	9.9	-145 – 240	31.2	GASS	-10.4	Blue
J0958+3204	33737	149.714	32.073	0.0270	8103	10.7	12.3	269	10.0	-412 – -146	31.6	GASS	<-12.7	Red
J1002+3238	33777	150.711	32.645	0.0477	14300	10.1	11.6	162	<8.9	–	9.1	GASS	-11.9	Red
J1013+0501	8634	153.352	5.025	0.0464	13916	10.1	11.6	165	9.5	-187 – 200	17.2	GASS	-10.8	Blue
J1032+2112	55541	158.196	21.216	0.0429	12852	10.6	12.2	245	9.9	-218 – 200	28.3	GASS	-10.1	Blue
J1051+1245	23419	162.827	12.757	0.0400	11982	10.4	11.9	194	10.0	-214 – 108	33.6	ALFALFA	-10.0	Blue
J1059+0517	9109	164.811	5.292	0.0353	10591	11.1	13.3	563	<9.0	–	9.7	GBT	-11.9	Red
J1100+1210	23457	165.048	12.171	0.0354	10606	10.1	11.6	164	<8.7	–	6.6	GASS	-10.7	Blue
J1100+1043	23477	165.200	10.728	0.0360	10798	11.1	13.3	601	9.9	–	29.4	ALFALFA	-11.0	Blue
J1115+0241	5701	168.789	2.699	0.0442	13262	10.7	12.4	284	9.8	-237 – 227	27.6	GASS	-10.9	Blue
J1120+0410	12452	170.026	4.177	0.0492	14746	10.8	12.6	332	<9.1	–	10.6	GASS	<-12.1	Red
J1122+0314	5872	170.642	3.244	0.0446	13358	10.5	12.0	222	<9.2	–	12.6	GBT	-12.0	Red
J1127+2657	48604	171.943	26.960	0.0334	10001	10.6	12.1	239	9.8	-187 – 206	25.6	GASS	-11.0	Blue
J1131+1553	29898	172.954	15.897	0.0364	10924	10.2	11.7	169	<9.0	–	10.1	GBT	-12.0	Red
J1132+1329	29871	173.052	13.492	0.0342	10267	10.2	11.7	168	9.8	-256 – 251	25.0	ALFALFA	-9.7	Blue
J1142+3013	48994	175.575	30.230	0.0322	9665	10.7	12.4	287	10.3	-196 – 227	49.4	GASS	-10.4	Blue
J1155+2921	49433	178.903	29.351	0.0458	13718	10.5	11.9	205	9.3	-148 – 162	13.6	GASS	-10.3	Blue
J1241+2847	50550	190.367	28.791	0.0350	10498	10.3	11.8	180	9.4	-125 – 177	16.4	GASS	-10.0	Blue
J1251+0551	13074	192.894	5.864	0.0486	14572	10.9	12.6	353	10.2	-257 – 291	41.5	ALFALFA	-10.4	Blue
J1305+0359	13159	196.356	3.992	0.0437	13094	10.4	11.8	191	9.4	-127 – 262	15.6	GASS	-10.8	Blue
J1315+1525	26936	198.855	15.423	0.0266	7959	10.7	12.4	294	<8.9	–	9.1	GASS	<-12.3	Red
J1317+2629	51025	199.440	26.486	0.0450	13490	10.3	11.7	176	9.8	-133 – 101	27.6	ALFALFA	-10.4	Blue
J1325+2714	51161	201.345	27.249	0.0345	10336	10.1	11.7	166	9.5	-123 – 183	18.1	GASS	-9.8	Blue
J1348+2453	38018	207.142	24.891	0.0297	8903	10.1	11.6	160	9.5	-173 – 173	17.0	GASS	-10.5	Blue
J1354+2433	44856	208.546	24.556	0.0286	8583	10.1	11.6	158	9.3	-160 – 187	13.3	GASS	-11.8	Red
J1404+3357	31172	211.122	33.953	0.0264	7920	10.3	11.8	181	9.5	-193 – 232	17.2	CHA	<-12.3	Red
J1406+0154	7121	211.678	1.915	0.0472	14153	10.2	11.7	175	8.9	-188 – 144	8.7	GASS	-11.8	Red
J1427+2629	45940	216.954	26.484	0.0325	9734	10.4	11.9	200	<8.7	–	6.7	GASS	-12.0	Red
J1430+0323	9615	217.508	3.398	0.0333	9983	10.2	11.7	166	9.4	-133 – 154	16.2	GASS	-11.1	Red
J1431+2440	38198	217.894	24.682	0.0378	11338	10.7	12.2	256	9.7	-211 – 247	23.2	GASS	<-12.7	Red
J1454+3050	42191	223.516	30.846	0.0320	9584	10.1	11.6	164	8.8	-173 – 97	7.8	GASS	-9.8	Blue
J1502+0649	41743	225.517	6.823	0.0462	13859	10.5	11.9	204	9.6	-166 – 186	20.5	GASS	-10.2	Blue
J1509+0704	41869	227.340	7.078	0.0414	12414	10.1	11.7	166	9.3	-133 – 176	14.0	GASS	-9.6	Blue
J1515+0701	42025	228.781	7.021	0.0367	11005	10.9	12.7	368	9.5	-206 – 205	17.5	GASS	-11.9	Red
J1541+2813	28365	235.344	28.230	0.0321	9620	10.4	11.8	189	10.1	-63 – 103	36.2	CHA	-9.6	Blue
J1544+2740	28317	236.034	27.673	0.0316	9482	10.1	11.6	160	9.1	-19 – 191	10.9	GASS	<-12.1	Red

<sup>a</sup> Systemic velocity,  $V_{\text{sys}}$ , is the velocity corresponding to the redshift of the galaxy i.e.  $V_{\text{sys}} = cz$ , where  $c$  is the speed of light in vacuum.

<sup>b</sup> Using prescription from Behroozi et al. 2010 (Eq. 21).

<sup>c</sup> The full width of the HI 21cm line in the rest-frame of the galaxy. The systemic velocity was subtracted from the observed HI velocity to obtain the rest-frame velocity.

<sup>d</sup> Using empirical relationship relating  $M_{\text{HI}}$  and  $R_{\text{HI}}$  as prescribed by Swaters et al. (2002).

<sup>e</sup> Values are from Schiminovich et al. (2010); Catinella et al. (2010). Values for sSFR  $< 10^{-12}$  yr $^{-1}$  are regarded as upper limits (discussed in Schiminovich et al. 2010).

<sup>f</sup> Galaxies with sSFR  $> 10^{-11}$  yr $^{-1}$  are defined as blue galaxies. Galaxies with sSFR below this value are identified as red galaxies.

TABLE 2  
DESCRIPTION OF QSO SIGHTLINES.

QSO	RA <sub>QSO</sub>	Dec <sub>QSO</sub>	z <sub>QSO</sub>	Galaxy	$\rho$ (kpc)	$\rho/R_{\text{vir}}$	$\Theta^a$	$W_{\text{Ly}\alpha}$ (Å)	$W_{\text{Ly}\alpha}/\bar{W}_{\text{Ly}\alpha}$	$v_{\text{Ly}\alpha}^b$ (km s <sup>-1</sup> )	$\Delta v_{\text{Ly}\alpha}^c$ (km s <sup>-1</sup> )	$v_{\text{HI}}^d$ (km s <sup>-1</sup> )	$v_{\text{esc},\rho}^e$ (km s <sup>-1</sup> )	$v_{\text{esc},R_{\text{vir}}}^e$ (km s <sup>-1</sup> )
J0159+1345	29.971	13.765	0.504	J0159+1346	102	0.6	64	1.501±0.023	2.975	93,358	-150 – 380	147	178	150
J0808+0514	122.162	5.244	0.361	J0808+0512	215	0.7	7	—	—	—	—	—	348	300
J0852+0313	133.247	3.222	0.297	J0852+0309	178	1.0	67	0.113±0.015	0.322	50	0 – 110	143	165	165
J0909+3236	137.276	32.608	0.809	J0908+3234	170	0.8	21	0.090±0.014	0.213	101	50 – 200	—	212	195
J0914+0837	138.632	8.629	0.649	J0914+0836	189	1.2	69	0.104±0.020	0.370	30	-50 – 80	108	133	143
J0930+2848	142.508	28.816	0.487	J0930+2853	214	1.0	42	<0.126	<0.372	—	—	—	189	191
J0931+2628	142.820	26.480	0.778	J0931+2632	226	0.5	77	0.114±0.013	0.199	200	150 – 250	—	541	423
J0936+3207	144.016	32.119	1.150	J0936+3204	160	0.9	0 <sup>f</sup>	<0.113	<0.280	—	—	—	183	172
J0937+1700	144.279	17.006	0.506	J0937+1658	63	0.2	64	0.135±0.021	0.168	-204	-300 – -150	-151	669	370
J0951+3542	147.850	35.714	0.398	J0951+3537	226	1.0	3	0.839±0.014	2.382	64	-90 – 200	240	212	211
J0959+3203	149.812	32.066	0.564	J0958+3204	162	0.6	0 <sup>f</sup>	0.420±0.016	0.815	-238,-144	-320 – -100	-412	298	249
J1002+3240	150.727	32.678	0.829	J1002+3238	119	0.7	40	<0.063	<0.140	—	—	—	166	149
J1013+0500	153.325	5.009	0.266	J1013+0501	102	0.6	0 <sup>f</sup>	0.445±0.024	0.875	-72	-180 – 50	-187	179	151
J1033+2112	158.270	21.204	0.315	J1032+2112	214	0.9	45	0.437±0.033	1.104	-1	-100 – 95	-218	238	227
J1051+1247	162.857	12.796	1.281	J1051+1245	140	0.7	73	0.781±0.022	1.706	-37	-180 – 140	-214	201	178
J1059+0519	164.795	5.327	0.754	J1059+0517	95	0.2	30	0.270±0.022	0.340	6	-100 – 100	—	932	525
J1059+1211	164.984	12.198	0.993	J1100+1210	171	1.0	61	0.225±0.014	0.676	-61	-150 – 0	—	148	151
J1100+1046	165.199	10.770	0.422	J1100+1043	108	0.2	0 <sup>f</sup>	—	—	—	—	—	980	562
J1115+0237	168.782	2.633	0.567	J1115+0241	209	0.7	83	0.195±0.020	0.430	2	-100 – 100	227	293	263
J1120+0413	170.021	4.223	0.545	J1120+0410	162	0.5	78	0.830±0.018	1.434	201,370	50 – 390	—	396	308
J1122+0318	170.601	3.301	0.475	J1122+0314	221	1.0	0 <sup>f</sup>	0.110±0.018	0.315	67	0 – 150	—	205	204
J1127+2654	171.902	26.914	0.379	J1127+2657	140	0.6	26	0.705±0.021	1.342	-28,-178	-250 – 100	-187	267	220
J1131+1556	172.905	15.946	0.183	J1131+1553	176	1.0	0 <sup>f</sup>	—	—	—	—	—	153	155
J1132+1335	173.044	13.586	0.201	J1132+1329	230	1.4	5	0.319±0.017	1.318	57	-40 – 130	251	138	155
J1142+3016	175.551	30.270	0.481	J1142+3013	104	0.4	50	0.886±0.023	1.351	3	-200 – 170	227	376	265
J1155+2922	178.970	29.377	0.520	J1155+2921	208	1.0	1	0.742±0.023	2.156	72,-150	-200 – 230	162	188	189
J1241+2852	190.374	28.870	0.589	J1241+2847	198	1.1	40	0.211±0.020	0.667	33	-120 – 170	177	160	166
J1251+0554	192.853	5.906	1.377	J1251+0551	200	0.6	57	0.409±0.021	0.765	80	-20 – 180	291	401	328
J1305+0357	196.351	3.959	0.545	J1305+0359	103	0.5	11	0.821±0.016	1.494	67,-43	-160 – 180	262	218	175
J1315+1525	198.938	15.432	0.448	J1315+1525	155	0.5	17	0.405±0.018	0.728	64	-50 – 170	—	341	272
J1318+2628	199.508	26.475	1.234	J1317+2629	198	1.1	86	0.184±0.032	0.597	0	-120 – 120	-133	155	162
J1325+2717	201.266	27.289	0.522	J1325+2714	199	1.2	55	—	—	—	—	—	143	153
J1348+2456	207.093	24.947	0.293	J1348+2453	153	1.0	81	0.474±0.035	1.301	-97	-230 – 0	-173	150	147
J1354+2430	208.604	24.502	1.878	J1354+2433	155	1.0	78	0.545±0.034	1.537	-97,-5	-170 – 50	-160	147	146
J1404+3353	211.118	33.895	0.549	J1404+3357	111	0.6	57	0.749±0.027	1.469	-26	-150 – 150	-193	198	166
J1406+0157	211.732	1.954	0.427	J1406+0154	222	1.3	67	—	—	—	—	—	147	161
J1427+2632	216.898	26.537	0.364	J1427+2629	170	0.9	0 <sup>f</sup>	—	—	—	—	—	195	184
J1429+0321	217.420	3.357	0.253	J1430+0323	231	1.4	0 <sup>f</sup>	0.807±0.027	3.414	-39,109	-150 – 250	-133	135	153
J1431+2442	217.858	24.706	0.407	J1431+2440	110	0.4	18	0.569±0.015	0.929	73,156	0 – 220	247	317	236
J1454+3046	223.601	30.783	0.465	J1454+3050	223	1.4	37	0.472±0.035	1.941	57	-50 – 160	97	134	151
J1502+0645	225.517	6.754	0.288	J1502+0649	224	1.1	80	0.438±0.013	1.384	12,-55	-150 – 110	186	182	188
J1509+0702	227.368	7.043	0.418	J1509+0704	130	0.8	62	0.956±0.022	2.220	49,-18,-215	-275 – 130	176	167	153
J1515+0657	228.781	6.952	0.268	J1515+0701	180	0.5	14	0.270±0.023	0.468	-367	-500 – -300	-206	439	342
J1541+2817	235.340	28.285	0.376	J1541+2813	128	0.7	0 <sup>f</sup>	0.864±0.011	1.797	-363	-520 – -250	-63	200	174
J1544+2743	236.114	27.723	0.163	J1544+2740	196	1.2	55	0.191±0.022	0.687	126	50 – 210	191	136	147

<sup>a</sup> Orientation of the QSO sightlines with respect to the disk of the galaxies. The values are based on SDSS r-band photometric measurements.

<sup>b</sup> Centroid of the multiple components of the Ly $\alpha$  absorption feature as estimated via Voigt profile fitting in the order of the strength of the component.

<sup>c</sup> Full width of the absorption feature in the rest-frame of the galaxy.

<sup>d</sup> Maximum velocity of the HI profile in the rest-frame of the galaxy. This value was measured on the velocity side where the centroid of the Lyman  $\alpha$  absorber was detected.

<sup>e</sup> Line of sight escape velocity at the impact parameter probed by the QSO sightline assuming a NFW profile for the galaxy's dark matter distribution.

<sup>f</sup> Face-on galaxies.

